

# A Radiomics-Boosted Deep-Learning Model for COVID-19 and Non-COVID-19 Pneumonia Detection Using Chest X-ray Image

Zongsheng Hu<sup>1</sup>, Zhenyu Yang<sup>2</sup>, Kyle J. Lafata<sup>2,3</sup>, Fang-Fang Yin<sup>1,2</sup>, Chunhao Wang<sup>\*2</sup>

<sup>1</sup>Medical Physics Graduate Program, Duke Kunshan University, Kunshan, Jiangsu, China 215316

<sup>2</sup>Department of Radiation Oncology, Duke University, Durham, NC, 27710

<sup>3</sup>Department of Radiology, Duke University, Durham, NC, 27710

Running Head: Radiomics-boosted COVID-19 detection

\*Corresponding authors:

Chunhao Wang, Ph.D.

Department of Radiation Oncology

Duke University Medical Center

Durham, NC, 27710, United States

E-mail: [chunhao.wang@duke.edu](mailto:chunhao.wang@duke.edu)

# Abstract

## Purpose:

To develop a deep-learning model that integrates radiomics analysis for enhanced performance of COVID-19 and Non-COVID-19 pneumonia detection using chest X-ray image

## Methods:

Based on a pre-trained VGG-16 architecture, the deep-learning design consists of a 5-Dense layer neural network with varying sizes, while the last three convolutional layers were set as free parameters for training. In radiomics analysis, a 2D sliding kernel was implemented to map the impulse response of radiomic features throughout the entire X-ray image; thus, each feature is rendered as a 2D map in the same dimension as X-ray image. Two deep-learning models were trained: in the 1<sup>st</sup> model, X-ray image was the sole input; in the 2<sup>nd</sup> model, X-ray image and 2 radiomic feature maps (RFM) selected by the saliency map analysis of the 1<sup>st</sup> model were stacked as the input.

Both models were developed using 812 chest X-ray images with 262/288/262 COVID-19/Non-COVID-19 pneumonia/healthy cases, and 649/163 cases were assigned as training-validation/independent test sets. For each model design, 50 versions were trained with random assignments of training/validation cases following 7:1 ratio in the training-validation set. Sensitivity, specificity, accuracy, and ROC curves were compared between the two designs.

## Results:

In 1<sup>st</sup> model using X-ray as the sole input, the 1) sensitivity, 2) specificity, 3) accuracy, and 4) ROC Area-Under-the-Curve of COVID-19 vs Non-COVID-19 pneumonia detection were 1)  $0.90 \pm 0.07$  vs  $0.78 \pm 0.09$ , 2)  $0.94 \pm 0.04$  vs  $0.94 \pm 0.04$ , 3)  $0.93 \pm 0.03$  vs  $0.89 \pm 0.03$ , and 4)  $0.96 \pm 0.02$  vs  $0.92 \pm 0.04$ . In the 2<sup>nd</sup> model, two RFMs, Entropy and Short-Run-Emphasize, were selected with their highest cross-correlations with the saliency maps of the 1<sup>st</sup> model. The corresponding results demonstrated significant improvements ( $p < 0.05$ ) of COVID-19 vs Non-COVID-19 pneumonia detection: 1)

0.95±0.04 vs 0.85±0.04, 2) 0.97±0.02 vs 0.96±0.02, 3) 0.97±0.02 vs 0.93±0.02, and 4) 0.99±0.01 vs 0.97±0.02. The reduced variations suggested a superior robustness of 2<sup>nd</sup> model design.

#### Conclusions:

The inclusion of radiomic analysis in deep-learning design improved the performance and robustness of COVID-19/Non-COVID-19 pneumonia detection, which holds great potential for clinical applications in the COVID-19 pandemic.

#### Key Words:

COVID-19, deep learning, radiomics, x-ray

## Introduction

Since its first discovery in 2019, the coronavirus disease (COVID-19) has affected more than 100 million people globally, and 2.7 million deaths related to COVID-19 were reported by April 1<sup>st</sup>, 2021<sup>1</sup>. Accurate and efficient diagnosis of COVID-19 infection is crucial to interrupt disease transmission and to start treatments of affected individuals. Currently, reverse transcription polymerase chain reaction (RT-PCR) has been recognized as the gold standard for COVID-19 affection diagnosis for its high specificity<sup>2</sup>. While RT-PCR test may have limited sensitivity and longtime of processing (a few hours to 2 days)<sup>3</sup>, radiographic procedures, including chest X-ray and CT exams, have been adopted clinically as alternative diagnosis tools<sup>4</sup>. While COVID-19 related abnormalities could be more easily found in volumetric CT images<sup>5</sup>, planar chest X-ray has its unique advantages in COVID-19 diagnosis. Specifically, the short imaging time on a more accessible X-ray unit enables rapid COVID-19 exams, which can be critical in areas with high-volume patients and/or limited-resource medical facilities. To date, pilot studies have revealed that certain X-ray image features, including peripheral consolidations and ground-glass opacities, have been widely observed in COVID-19 infected patients<sup>4-9</sup>. However, the prevalent application of chest X-ray imaging in COVID-19 diagnosis is challenged by relatively limited sensitivity and specificity<sup>5</sup>. Additionally, radiographic exams including chest X-ray may not be optimal for radiologists' reading in the differentiation of non-COVID-19 pneumonia from COVID-19 infections, which is important for early patient stratification that can lower COVID-19 mortality rate with more targeted treatments<sup>10,11</sup>.

Computed aided diagnosis systems (CAD) may have the potential to solve the aforementioned problem with high throughput quantitative analysis. In the last several months under the COVID-19 pandemic, studies revealed that CAD systems outperformed radiologists in radiographic-based COVID-19 diagnosis; with CAD information as reference information, radiologist reading results could be significantly improved<sup>11-13</sup>. One approach for such CAD system is radiomics-based image analysis, which first extracts radiomics features as computation image biomarkers and then uses the extracted features in hand-made or machine learning classifier tasks. Although handcrafted radiomics features are commonly used in medical image analysis with possible qualitative image interpretability, the

reported accuracy (75-80%) of COVID-19 diagnosis is still limited in the representative radiomics-based CAD works<sup>14-16</sup>. Driven by recent theoretical developments and accesses to massive computation power, deep learning has demonstrated its great potential in CAD developments. It has been reported that deep learning solution based on artificial neural network deployment could achieve high (>90%) specificities in COVID-19 diagnosis against healthy individuals<sup>17,18</sup>; moreover, decent specificities (>85%) of differentiating COVID-19 affection from non-COVID-19 pneumonia have been achieved<sup>11,19</sup>. Nevertheless, like all other deep learning applications in medical image analysis, the hyperparameters in the neural network are generated without explicit human knowledge intervention. Thus, the ‘black box’ nature of deep learning-based CAD inhibits their interpretability, and potential clinical applications of these CADs could be impaired by limited interpretability by clinicians.

In this work, we aim to develop a radiomics-boosted deep learning CAD design for chest X-ray based COVID-19 diagnosis. Based on a custom-trained neural network, the CAD can classify COVID-19 infections, non-COVID-19 pneumonia, and healthy individuals. An innovative implementation of radiomics analysis was included to analyze neural network parameters, and the analysis results were used to incorporate novel radiomics results in image rendering as neural network inputs. Thus, the achieved radiomics-boost deep learning can be better interpreted by qualitative image descriptions within in current clinician knowledge domain.

## Materials and Methods

### *Image Dataset*

In this IRB-waived retrospective study, a total of 812 chest X-ray images were collected from three public databases<sup>20-22</sup>, including 262/288/262 images of COVID-19/Non-COVID-19 pneumonia/healthy individuals, respectively. The image numbers from the three categories were approximately the same for eliminating categorical bias during deep learning training. All collected images were verified by experienced medical physicists with proper lung X-ray display settings and no overlaid image reading annotations. To unify image data size, all images were resized to a 256x256 matrix grid size using b-spline interpolation and were normalized to 256 gray levels. 649 and 163 images (8:2) were assigned for the model training set and the independent test set, respectively.

### *Neural Network Architecture*

Figure 1 illustrates the deep learning neural network architecture of this work. This design was mainly constructed based on a pre-trained VGG-16 architecture<sup>23</sup>. The input is a three-channel image with a 256×256×3 shape size. For each convolutional layer, the filter size is 3×3 with padding and stride of 1. Max-pooling is performed over a 2x2-pixel window, with a stride of 2. The self-defined dense classifier connects with convolutional base and consists of five Dense layers with the size of 1024, 1024, 512, 256, and 3, respectively. The output of neural network is one of the three categorical binary label vectors, i.e., [1,0,0]/ [0,1,0]/ [0,0,1], which correspond to COVID-19/Non-COVID-19 pneumonia/healthy results, respectively. To deal with relatively small data size in this work, the convolutional base loaded the weights that were pre-trained on ImageNet as a transfer learning scheme<sup>24</sup>. Fine-tune technique was used with the last three convolutional layers (marked \* in Figure 1) being set as free parameters for custom training. To avoid the occurrence of overfitting, a dropout layer was added between the first two Dense layers with a dropout possibility of 0.5, and soft-max activation was used in the output layer.

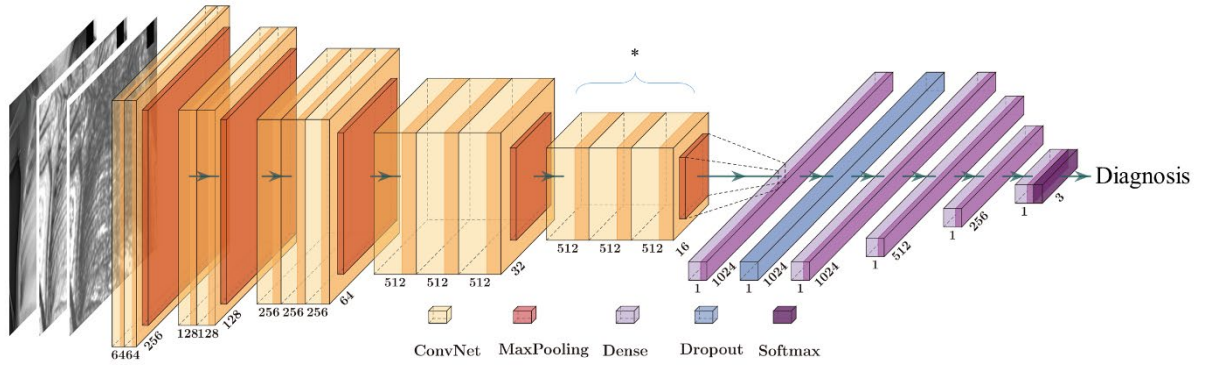


Figure 1. Deep learning network diagram.

### *Radiomic Feature Map Extraction*

Classic radiomics analysis calculates radiomic features as scalar values from a pre-defined region-of-interest (ROI) in image space. While this approach has been widely adopted to capture the overall textures in ROI, it cannot capture the anatomy-driven subtle texture variations within the ROI. As such, we implement a radiomic feature map calculation workflow, which is summarized in Figure 2. Specifically in this work, a 2D sliding kernel (13x13 matrix size) was adopted to extract a local region centered at a pixel-of-interest. Scalar feature values were derived within the extracted local region (dashed arrow). By iterating this calculation throughout the whole X-ray image (green arrow), radiomic feature maps (RFMs) in image renderings are derived with the same dimension as X-ray image. In this work, 37 RFMs were calculated for each X-ray image, including 21 RFMs of grey level co-occurrence matrix (GLCOM) radiomic features and 16 RFMs of grey level run-length matrix (GLRLM) radiomic features.

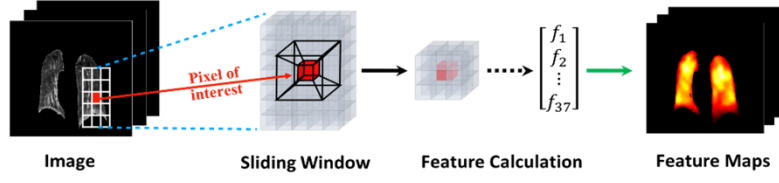


Figure 2. A workflow summary of radiomic feature map (FM) calculation in this work.

### Model Training and Evaluation

Two deep learning models were developed following the neural network architecture in Figure 1. In the 1<sup>st</sup> model, the X-ray image is the sole model input. To accommodate the VGG-16 data shape, the grayscale X-ray images were broadcast to three channels as a network input variable. This model serves as the benchmarking deep learning model in this work. In the 2<sup>nd</sup> radiomics-boosted deep learning model, the grayscale X-ray image and two derived RFMs were stacked as the 3-channel neural network input variable. These two RFMs were selected based on the analysis of the 1<sup>st</sup> model's saliency map (SM), which indicates how important each pixel is with respect to the final classification results of the neural network in the benchmarking model. It is calculated as the absolute gradient of class activation, which is defined as the dot product of prediction output and target divided by the input image<sup>25</sup>: a pixel with a higher value in SM indicates higher importance of that pixel in neural network's attention for diagnosis. The two RFMs (one in each feature category) with the highest average cross-correlation (CC) values against the SM results in training data were selected. This action amplifies certain pixels (and regions) with potentially high importance of disease diagnosis in the image space, which could improve the overall diagnostic accuracy of the proposed radiomics-boosted model in comparison with the 1<sup>st</sup> benchmarking model.

To investigate the robustness of the two developed models, 50 versions of each model design were trained using the training data set (649 images). In each version, the training and validation samples were randomly selected following a 7:1 ratio. During deep learning training, the loss function was categorical cross-entropy, and Adam optimizer was selected. The training time was about 15 minutes in a TensorFlow environment using an Nvidia Tesla V100 graphic card. For model evaluation,



sensitivity, specificity, accuracy, and ROC area under the curve (AUC) results from both models were analyzed. Statistical significance of comparison was determined by Wilcoxon signed rank tests at level 0.05

## Results

Based on the saliency map analysis of the 1<sup>st</sup> deep learning model, two RFMs, GLCOM Entropy (cc=0.33) and GLRLM Short Run Emphasis (SRE) (cc=0.31) were found to have the highest CC among their categories, respectively. The stack of two selected RFMs and original X-ray was used for radiomics-boosted deep learning model inputs. Figure 3 shows the identified RFMs from three example patients. As illustrated, the RFMs render more tissue textural variations in both lung and other soft tissue regions.

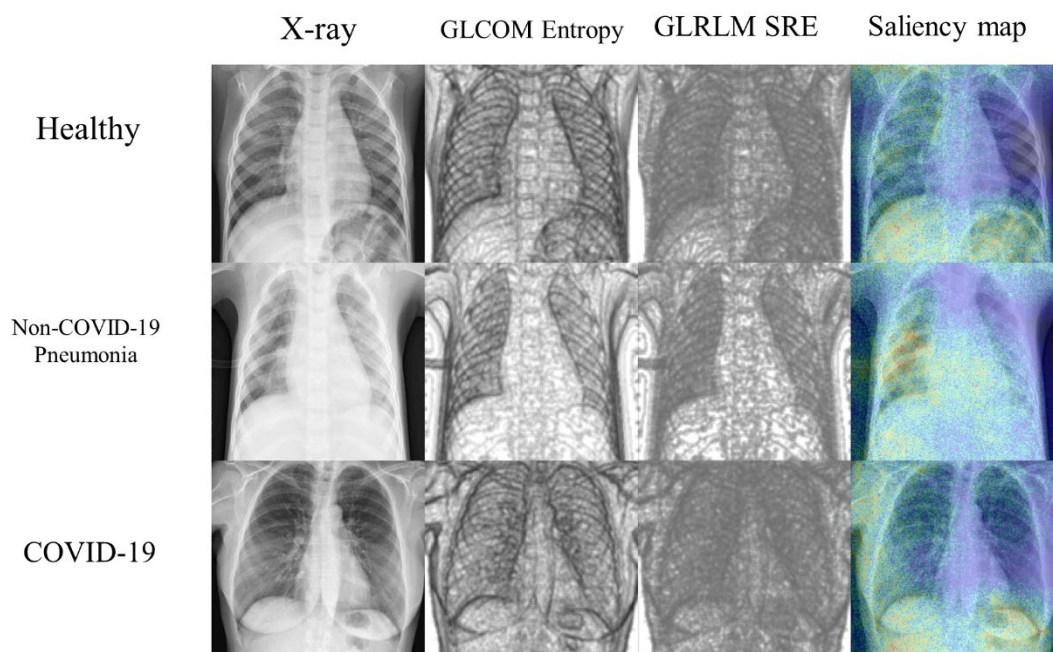


Figure 3. Image comparisons from 3 example cases. The GLRLM SRE RFMs and saliency map (overlaid with X-ray image) are illustrated in 0.3 power scale.

Figure 4 summarizes the ROC analysis results for two models. The blue and red solid lines represent the average ROC results of 50 versions of two deep learning model designs (X-ray only vs. X-ray + RFM), and the colored bands represent the model performance variation of 50 versions as  $\pm 1$  standard deviation. As demonstrated, the average result of the radiomics-boost deep learning model (X-ray + RFM) outperformed the model using X-ray only. The largest performance improvement is observed

in Non-COVID-19 pneumonia diagnosis. Additionally, the radiomics-boost deep learning model has narrower ROC band width, which suggests the enhanced robustness of its design under different data sample uses.

Table 1 summarizes the quantitative comparisons of sensitivity, specificity, accuracy, and ROC AUC between two tested DL models. In general, the radiomics-boost deep learning model achieved statistical improvements in all parameters with  $p < 0.05$ . The largest improvements were observed in non-COVID-19 pneumonia diagnosis. Additionally, the reduced standard deviations of the reported statistics indicated the enhanced robustness of radiomics-boost deep learning design. These quantitative results highlight the superiority of the proposed radiomics-boost deep learning model design. It worth mentioning that the developed radiomics-boost deep learning model achieved the best performance in COVID-19 diagnosis. For COVID-19 diagnosis, the developed radiomics-boost deep learning model achieved higher sensitivity (94.9%), specificity (97.3%), accuracy (96.5%), and AUC(99.3%) compared to model 1. The standard variation of 50 versions is less than 3%, reaching a high level of robustness. The performance demonstrates the potential of enhancing the accuracy and efficiency of COVID-19 diagnosis in clinical application by incorporating radiomics information in DL model.

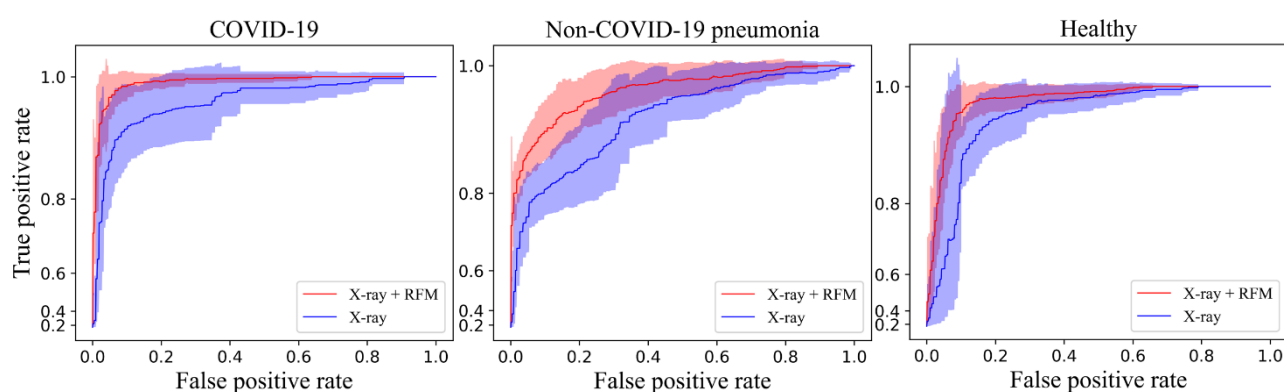


Figure 4. The ROC results from 2 different deep learning model design. 0.3 power scale was used in y axis to highlight the difference.

	Healthy		Non-COVID-19 pneumonia		COVID-19	
	X-ray	X-ray+RFM	X-ray	X-ray+RFM	X-ray	X-ray+RFM
Sensitivity	0.854±0.065	0.922±0.059	0.780±0.092	0.857±0.0361	0.903±0.071	0.949±0.036
Specificity	0.918±0.044	0.938±0.022	0.941±0.041	0.963±0.023	0.940±0.037	0.973±0.020
Accuracy	0.895±0.029	0.933±0.023	0.892±0.029	0.931±0.016	0.927±0.028	0.965±0.016
AUC	0.948±0.027	0.979±0.012	0.918±0.043	0.969±0.017	0.963±0.023	0.993±0.006

Table 1. Sensitivity, specificity, accuracy, and ROC AUC results summary. Mean value and standard deviation of 50 trained versions are reported. All comparisons were statistically significant

The SMs results of the radiomics-boosted deep learning model are illustrated in the last column of Figure 3. The pixel values in SM can be interpreted as the attention of the deep learning model. As seen, the attention patterns, i.e., colored hot regions distribution in SMs, were different in different patient cohorts: the model may have more attention to lateral lung regions for COVID-19 detection, while it may have more attention to the mediastinum regions for non-COVID-19 pneumonia detection. In order to quantitatively analyze the attention patterns across different patient cohorts, we calculated the CC matrix of SMs in the test set in Figure 5, which includes all the CCs between SMs of 2 samples from the test set. As summarized, CCs within each cohort were relatively higher than those calculated across different cohort. This result suggests that the developed deep learning model captured cohort-specific features for the classification task. Additionally, the mean CC result of COVID-19 vs Non-COVID-19 pneumonia (0.12) cohort was slightly higher than the result of COVID-19 vs Healthy cohorts (0.07) and Non-COVID-19 pneumonia vs Healthy cohorts (0.09). This observed COVID-19/Non-COVID-19 pneumonia similarity supports the clinical reports of challenges in COVID-19/Non-COVID-19 pneumonia differentiation<sup>10,11</sup>.

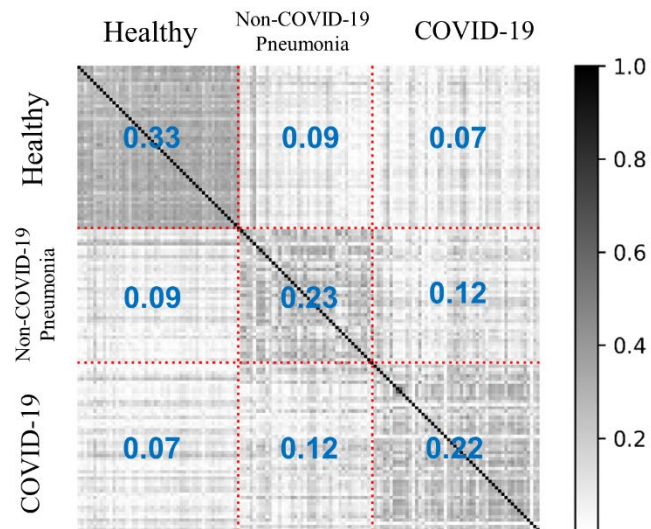


Figure 5. The cross-correlation matrix of SMs of 2nd model on test set. The x and y axis represents the sample ID in test set, sorting with the order of healthy/Non-COVID-19 pneumonia/COVID-19 cohorts.

## Discussion

To our best knowledge, this work is the first of its kind for combining radiomics analysis and deep neural network implementation. The results of this work proved that the inclusion of radiomic feature maps, as a new form of handcrafted imaging biomarker rendering, can improve deep learning-based COVID-19 detection. With the aid of RFMs, we achieve higher model performance (a sensitivity of 92.2%/85.7%/94.9%, a specificity of 93.8%/96.3%/97.3%, and an accuracy of 93.3%/93.1%/96.5% for Healthy/non-COVID-19 pneumonia/COVID-19) with a smaller (812 patients in total) than reported work. For example, Zhang et al.<sup>11</sup> achieve a sensitivity of 88% and a specificity of 79% in COVID-19/non-COVID-19 pneumonia diagnosis with a dataset of 2060 patients. Nishio et al.<sup>19</sup> achieve an accuracy of 83.7% for 3 categories of classification (Healthy/non-COVID-19 pneumonia/COVID-19) using the VGG-16 model trained on 1248 images. In addition, the robustness of the developed model was systematically analyzed. For each model design, we trained 50 versions of models using randomly selected training and validation samples following a ratio of 7:1. The small standard deviations ( $< 0.06$ ) of selected metrics and ROC results revealed the enhanced robustness of the developed model, which further demonstrates the potential of the radiomics-boosted deep learning design in clinical situations using different X-ray image data sources.

The inclusion of radiomic feature maps (RFMs) is another key technical innovation of this work. Instead of calculating radiomic features as scalar values from selected volumes in image space, RFMs capture the anatomy-driven subtle texture variations within ROIs. It has been proved that whole lung RFMs are correlated with lung ventilation measurement results<sup>26</sup>; as such, the potential functional information in RFMs contributes to the enhanced COVID-19 diagnosis accuracy. The selection of two RFMs from 37 RFMs is more than a trivial task: while direct comparisons of all possible RFM combinations are feasible, it requires huge computation loads without the potential of transferring this technique to other clinical applications. Driven by the hypothesis that certain RFMs can be related to neural network hyperparameters, we selected RFMs based on similarity metrics between RFMs and neural network saliency maps (SMs), which measures the attention pattern of network implementation. RFMs with higher similarities to SMs could emphasize regional information to enhance neural network

attention, which increases synchronously with SM results. In current clinical practice, mutual information (MI) and cross-correlation (CC) are two common image similarity metrics for image registration and classification. Figure 6 summarizes the top 8 RFM candidates in GLCOM and GLRLM feature categories with normalized MI and CC results. As seen, while RFMs were sorted by CC values, most of them had close normalized MI results, which might not be directly related to image difference appearance; Given these considerations, two RFMs, GLCOM Entropy (CC = 0.33) and GLRLM Short Run Emphasis (SRE) (CC = 0.31) from two feature categories were selected based on CC analysis. It would be of interest to investigate other RFM selection mechanisms that can be complementary to the current design.

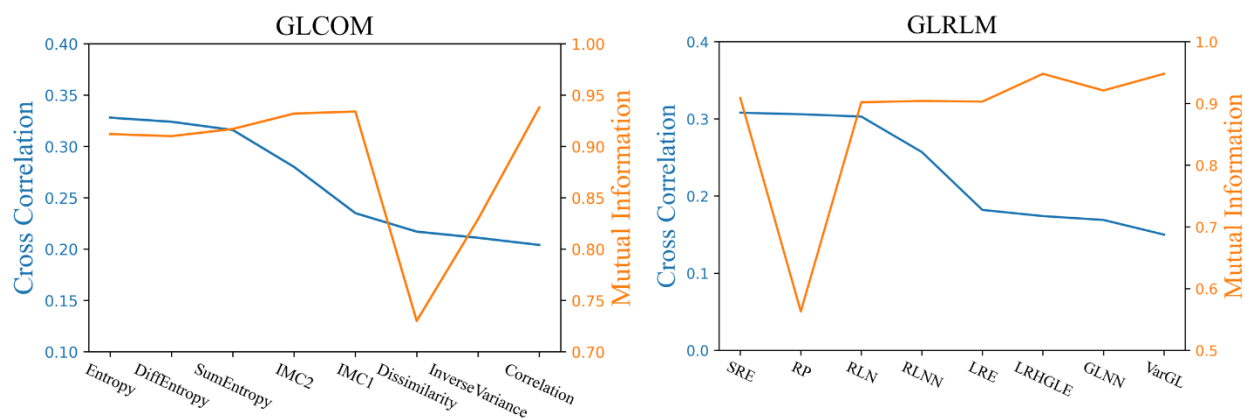


Figure 6 Normalized MI and CC results of top 8 RFM candidates ranked by CC results in GLCOM and GLRLM feature categories

The presented design of combining radiomics analysis and deep neural network implementation may create a new paradigm of computer aided diagnosis (CAD) system. The implemented RFM calculation workflow may also enhance neural network performance in other diagnosis tasks. Additionally, the proposed method provides a radiomics perspective of deep learning interpretability. The hyperparameters in the neural network are trained without explicit human knowledge intervention and thus are hard to interpret by empirical knowledge. For deep learning-based CAD systems, the ‘black box’ nature impaired the clinical deployments of such systems without clinicians’ confidence. As a step towards deep learning interpretability, we investigated neural network attention information using a radiomics-based analysis, while radiomics has been widely studied as computational imaging

biomarkers for disease detection and outcome monitoring. Following saliency map analysis approach in this work, additional parameters can be used to enhance deep learning interpretability, such as histology samples image from biopsy and anatomy contours from radiation therapy. These directions will be studied in future works when appropriate datasets become available.



## **Conclusion**

In this study, we proposed a radiomics-boosted deep learning design for X-ray based COVID-19 diagnosis and non-COVID-19 pneumonia diagnosis. An innovative radiomic feature map calculation workflow was implemented to generate inputs of a VGG-16 based neural network architecture. Results showed that the proposed radiomics-boosted deep learning design improved the performance and robustness of COVID-19 and Non-COVID-19 pneumonia detection in concurrence with a radiomics viewpoint of deep learning interpretation. It holds great potential for clinical applications for COVID-19 diagnosis and for other diseases.

## References

1. Worldometer. *COVID-19 CORONAVIRUS PANDEMIC*. <https://www.worldometers.info/coronavirus/>.
2. Wang W, Xu Y, Gao R, et al. Detection of SARS-CoV-2 in Different Types of Clinical Specimens [published online ahead of print 2020/03/12]. *JAMA*. 2020;323(18):1843-1844.
3. Fang Y, Zhang H, Xie J, et al. Sensitivity of Chest CT for COVID-19: Comparison to RT-PCR [published online ahead of print 2020/02/20]. *Radiology*. 2020;296(2):E115-E117.
4. Ai T, Yang ZL, Hou HY, et al. Correlation of Chest CT and RT-PCR Testing for Coronavirus Disease 2019 (COVID-19) in China: A Report of 1014 Cases. *Radiology*. 2020;296(2):E32-E40.
5. Yoon SH, Lee KH, Kim JY, et al. Chest Radiographic and CT Findings of the 2019 Novel Coronavirus Disease (COVID-19): Analysis of Nine Patients Treated in Korea [published online ahead of print 2020/02/27]. *Korean J Radiol*. 2020;21(4):494-500.
6. Xie X, Zhong Z, Zhao W, Zheng C, Wang F, Liu J. Chest CT for Typical Coronavirus Disease 2019 (COVID-19) Pneumonia: Relationship to Negative RT-PCR Testing [published online ahead of print 2020/02/13]. *Radiology*. 2020;296(2):E41-E45.
7. Wong HYF, Lam HYS, Fong AHT, et al. Frequency and Distribution of Chest Radiographic Findings in Patients Positive for COVID-19. *Radiology*. 2020;296(2):E72-E78.
8. Guan W, Ni Z, Hu Y, et al. Clinical Characteristics of Coronavirus Disease 2019 in China. *N Engl J Med*. 2020;382(18):1708-1720.
9. Shi HS, Han XY, Jiang NC, et al. Radiological findings from 81 patients with COVID-19 pneumonia in Wuhan, China: a descriptive study. *Lancet Infect Dis*. 2020;20(4):425-434.
10. Bai HX, Hsieh B, Xiong Z, et al. Performance of Radiologists in Differentiating COVID-19 from Non-COVID-19 Viral Pneumonia at Chest CT [published online ahead of print 2020/03/11]. *Radiology*. 2020;296(2):E46-E54.
11. Zhang R, Tie X, Qi Z, et al. Diagnosis of Coronavirus Disease 2019 Pneumonia by Using Chest Radiography: Value of Artificial Intelligence [published online ahead of print 2020/09/25]. *Radiology*. 2021;298(2):E88-E97.
12. Bai HX, Wang R, Xiong Z, et al. Artificial Intelligence Augmentation of Radiologist Performance in Distinguishing COVID-19 from Pneumonia of Other Origin at Chest CT [published online ahead of print 2020/04/28]. *Radiology*. 2020;296(3):E156-E165.
13. Wang H, Wang L, Lee EH, et al. Decoding COVID-19 pneumonia: comparison of deep learning and radiomics CT image signatures [published online ahead of print 2020/10/24]. *Eur J Nucl Med Mol Imaging*. 2020. doi: 10.1007/s00259-020-05075-4.

14. Fang X, Li X, Bian Y, Ji X, Lu J. Radiomics nomogram for the prediction of 2019 novel coronavirus pneumonia caused by SARS-CoV-2 [published online ahead of print 2020/07/06]. *Eur Radiol.* 2020;30(12):6888-6901.
15. Santone A, Belfiore MP, Mercaldo F, Varriano G, Brunese L. On the Adoption of Radiomics and Formal Methods for COVID-19 Coronavirus Diagnosis [published online ahead of print 2021/03/07]. *Diagnostics (Basel)*. 2021;11(2).
16. Wang L, Kelly B, Lee EH, et al. Multi-classifier-based identification of COVID-19 from chest computed tomography using generalizable and interpretable radiomics features [published online ahead of print 2021/01/27]. *Eur J Radiol.* 2021;136:109552.
17. Minaee S, Kafieh R, Sonka M, Yazdani S, Jamalipour Soufi G. Deep-COVID: Predicting COVID-19 from chest X-ray images using deep transfer learning [published online ahead of print 2020/08/12]. *Med Image Anal.* 2020;65:101794.
18. Khan AI, Shah JL, Bhat MM. CoroNet: A deep neural network for detection and diagnosis of COVID-19 from chest x-ray images [published online ahead of print 2020/06/14]. *Comput Methods Programs Biomed.* 2020;196:105581.
19. Nishio M, Noguchi S, Matsuo H, Murakami T. Automatic classification between COVID-19 pneumonia, non-COVID-19 pneumonia, and the healthy on chest X-ray image: combination of data augmentation methods [published online ahead of print 2020/10/18]. *Sci Rep.* 2020;10(1):17532.
20. Google. COVID-19 X-ray dataset. <https://drive.google.com/file/d/1AfC8emc3mGCfY01jK-R6suK7a2Kv2m2>.
21. Cohen J, Morrison P, Dao L. COVID-19 Image Data Collection. *arXiv.* 2020. doi: 2003.11597.
22. Paul M. Chest X-Ray Images (Pneumonia). <https://www.kaggle.com/paultimothymooney/chest-xray-pneumonia>.
23. Karen S, Andrew Z. Very Deep Convolutional Networks for Large-Scale Image Recognition. *arXiv.* 2014. doi: arXiv:1409.1556.
24. Deng J, Dong W, Socher R, et al. ImageNet: A Large-Scale Hierarchical Image Database. In: *Cvpr: 2009 Ieee Conference on Computer Vision and Pattern Recognition, Vols 1-4*. doi: 10.1109/cvpr.2009.5206848 New York: Ieee; 2009:248-255.
25. Karen S, Andrea V, Andrew Z. Deep Inside Convolutional Networks: Visualising Image Classification Models and Saliency Maps. *arXiv.* 2014. doi: arXiv:1312.6034v2.
26. Zhenyu Y, Kyle L, Xinru C, et al. Quantification of lung function on CT images based on pulmonary radiomic filtering. *arXiv.* 2021. doi: arXiv:2105.11171.



## Figure Captions

Figure 1. Deep learning network diagram.

Figure 2. A workflow summary of radiomic feature map (FM) calculation in this work.

Figure 3. Image comparisons from 3 example cases. The GLRLM SRE RFMs and saliency map (overlaid with X-ray image) are illustrated in 0.3 power scale.

Figure 4. The ROC results from 2 different deep learning model design. 0.3 power scale was used in y axis to highlight the difference.

Figure 5. The cross-correlation matrix of SMs of 2nd model on test set. The x and y axis represents the sample ID in test set, sorting with the order of healthy/Non-COVID-19 pneumonia/COVID-19 cohorts.

Figure 6 Normalized MI and CC results of top 8 RFM candidates ranked by CC results in GLCOM and GLRLM feature categories